Nickel Superoxide Dismutase Structure and Mechanism†

David P. Barondeau, Carey J. Kassmann, Cami K. Bruns,‡ John A. Tainer, and Elizabeth D. Getzoff*

Department of Molecular Biology, The Skaggs Institute for Chemical Biology, The Scripps Research Institute, 10550 North Torrey Pines Road, La Jolla, California 92037

Received February 25, 2004; Revised Manuscript Received March 22, 2004

ABSTRACT: The 1.30 Å resolution crystal structure of nickel superoxide dismutase (NiSOD) identifies a novel SOD fold, assembly, and Ni active site. NiSOD is a hexameric assembly of right-handed 4-helix bundles of up−down−up−down topology with N-terminal hooks chelating the active site Ni ions. This newly identified nine-residue Ni-hook structural motif (His-Cys-X-X-Pro-Cys-Gly-X-Tyr) provides almost all interactions critical for metal binding and catalysis, and thus will likely be diagnostic of NiSODs. Conserved lysine residues are positioned for electrostatic guidance of the superoxide anion to the narrow active site channel. Apo structures show that the Ni-hook motif is unfolded prior to metal binding. The active site Ni geometry cycles from square planar Ni(II), with thiolate (Cys2 and Cys6) and backbone nitrogen (His1 and Cys2) ligands, to square pyramidal Ni(III) with an added axial His1 side chain ligand, consistent with electron paramagentic resonance spectroscopy. Analyses of the three NiSOD structures and comparisons to the Cu,Zn and Mn/Fe SODs support specific molecular mechanisms for NiSOD maturation and catalysis, and identify important structure−function relationships conserved among SODs.

SODs[1] (EC 1.15.1.1) are ubiquitous metalloenzymes that catalyze the disproportionation of superoxide to peroxide and molecular oxygen through alternate oxidation and reduction of their catalytic metal ions (*1*, *2*). SODs are essential enzymes for protecting cells from the toxic products of aerobic metabolism. Many free radicals are scavenged by dioxygen to form superoxide, making SOD a master regulator of free radical balance and reactive oxygen species in cells (*3*). Superoxide is also generated by animal macrophages as part of the immune response and has been implicated as an agent in the aging process, inflammatory diseases, post-ischemic tissue injury, and a number of pathological conditions (*4*−*6*).

Two classes of SOD, CuZnSOD and MnSOD or FeSOD, have been extensively characterized through structural, biochemical, and computational analysis. CuZnSODs are homodimeric or monomeric β-barrel proteins (*7*) found in eukaryotes and some prokaryotes. Point mutants in human CuZnSOD are linked to the fatal neurodegenerative disease familial amyotrophic lateral sclerosis or Lou Gehrig's disease (*8*). CuZnSOD contains a dinuclear metal site with three trigonal His Cu ligands in the reduced state and a fourth, Zn-bridging, His ligand in the oxidized state. MnSOD and FeSOD are homologous homodimeric or homotetrameric proteins with a two-domain primarily α-helical fold (*9*−*12*). Three histidine residues, one aspartic acid, and a solvent molecule in trigonal bipyramidal geometry coordinate the Fe/Mn ion. MnSODs occur in eukaryotic mitochondria and the cytoplasm of prokaryotes. MnSOD expression is often induced with oxygen (*13*). In contrast, FeSOD is constitutively expressed (*13*) in the cytosols of prokaryotes, primitive eukaryotes, and some green plants. Recently, a completely distinct third SOD class that contains Ni (NiSOD) was discovered in *Streptomyces* (*14*, *15*) and cyanobacteria (*16*).

NiSOD is a product of the *sodN* gene, which encodes the protein plus a 14 amino acid N-terminal extension that is removed in the mature enzyme (*14*). NiSOD is a small 117 amino acid protein with no sequence homology to other SODs. NiSOD is reported to function as a tetramer (*14*) but to remain monomeric without nickel (*17*). In *Streptomyces coelicolor*, nickel levels enhance NiSOD expression, while repressing FeSOD levels (*18*). A putative signal peptidase gene lies directly upstream of *sodN* and is properly oriented for divergent transcription. X-ray spectroscopic and EPR studies suggest that *Streptomyces seoulensis* NiSOD contains oxidized Ni^{3+} with an axial nitrogen ligand (*17*). The proposed dinuclear Ni−Ni active site and thiolate ligation, derived from EXAFS data, are unprecedented in SODs (*17*). This novel class of SOD, with a different metal center and distinct protein fold, provides an experimental system to test the essential features required for SOD's critical biological function in reactive oxygen regulation. Thus, we undertook biochemical, spectroscopic, and crystallographic studies to elucidate the structure and mechanism of NiSOD and define its conserved and variable features relative to the well-characterized Cu,Zn and Mn/Fe SODs. Here, we report structures of the active Ni-bound enzyme at 1.30 Å resolution

† We thank the La Jolla Interfaces in Sciences and NIH Postdoctoral Fellowships (D.P.B.), NIH Grant (E.D.G.), and ESRF and ALS for support.

* To whom correspondence should be addressed. Tel: 858-784-2878. Fax: 858-784-2277. E-mail: edg@scripps.edu.

‡ Present address: Department of Biological Sciences, Stanford University, Stanford, CA 94305-5430.

[1] Abbreviations: CuZnSOD, copper- and zinc-containing superoxide dismutase; EPR, electron paramagnetic resonance; EXAFS, extended X-ray absorption fine structure; MAD, multiwavelength anomalous diffraction; MnSOD, manganese-containing superoxide dismutase; MPEG, methoxy poly(ethylene glycol); NHE, normal hydrogen electrode; NiSOD, nickel-containing superoxide dismutase; PDB, Protein Data Bank; RMSD, root mean square deviation; SOD, superoxide dismutase; FeSOD, iron-containing superoxide dismutase.

10.1021/bi0496081 CCC: $27.50
Published on Web 06/03/2004

Table 1: NiSOD Data Collection and Refinement Statistics

	MAD				
	peak	edge	remote	native	CN-treated (apo)
			data collection		
space group			$C222_1$	$P2_1$	$C222_1$
wavelength (Å)	0.97912	0.979311	0.911656	1.0000	1.549784
resolution (Å)	20.0−2.80	20.0−2.80	20.0−2.80	100.0−1.30	100−2.05
last shell (Å)[a]	2.90−2.80	2.90−2.80	2.90−2.80	1.35−1.30	2.12−2.05
observations	39 675	39 496	38 991	896 499	163 690
unique observations	9394	9344	9300	347 604	23 036
R_{sym} (%)[b]	7.7 (35.3)	5.9 (30.9)	5.9 (26.7)	5.5 (36.5)	6.5 (32.4)
completeness (%)	99.8 (99.6)	99.8 (99.3)	99.8 (99.7)	94.5 (79.8)	96.4 (85.4)
I/σI	20.2 (3.3)	21.6 (3.7)	22.2 (4.3)	18.5 (1.6)	24.9 (5.1)
Wilson B-factor (Å^2)			63	11	36
			refinement		
refinement parameters			10 684	119 964	11 068
R_{work}/R_{free} (%)[c]			23.5/29.2	15.8/20.1	21.7/24.6
RMS deviations from ideality					
bond length (Å)			0.013	0.011	0.013
bond angle (°)			1.4	1.3	1.3
average B-factor (Å^2)					
protein			47.1	14.0	48.1
solvent			36.9	29.8	53.0
Ni ions			NA	8.6	NA

[a] Values in parentheses are the statistics for the highest resolution shell of data. [b] $R_{sym} = \sum|I_{hkl} - |/\sum \langle I\rangle$, where $\langle I\rangle$ is the average individual measurement of I_{hkl}. [c] $R_{work} = (\sum|F_{obs} - F_{calc}|)/\sum|F_{obs}|$, where F_{obs} and F_{calc} are the observed and calculated structure factors, respectively.

and the apo protein at 2.05 Å resolution, probe azide and cyanide inhibition with EPR spectroscopy, and provide data and mechanisms for NiSOD maturation and superoxide catalysis.

MATERIALS AND METHODS

Experimental Preparation. We obtained *S. coelicolor* genomic DNA (ATCC 10147) from Loftland labs Limited (Gaithersburg, MD) and cloned the NiSOD gene (*14*) into pET vectors (Novagen). The N-terminal *Streptomyces* leader sequence was replaced with a methionine residue in the Met0 NiSOD construct (pET11a) and by the *Escherichia coli* pelB signal sequence in the pelB NiSOD construct (pET26b). DNA sequencing for the Met0 construct revealed one amino acid change, Leu85Met, from the published primary structure (*19*). This same Leu85Met mutation was incorporated into the pelB construct with the QuikChange method (Stratagene). BL21-CodonPlus(DE3)-RIL *E. coli* (Stratagene) were transformed with these plasmids and grown at 25 °C in 9 L batches to an optical density of 0.5 at 600 nm, and then, protein expression was induced with 0.2 mM isopropyl-β-D-thiogalactoside. To obtain Ni-bound protein, we added 0.2 mM $NiCl_2$ at induction. The bacteria cells were pelleted 6−12 h later and frozen in liquid nitrogen until purification.

Distinct protein purification strategies were developed for the Met0 and pelB NiSOD constructs. For the Met0 NiSOD construct, cells were disrupted by sonication. Proteins that were soluble in 40% and precipitated in 70% ammonium sulfate were dialyzed against 20 mM Tris, pH 8.0, and purified with POROS HQ (26 mm × 30 cm) (PerSeptive Biosystems, Inc.) and S-100 (26 mm × 60 cm) (Pharmacia) columns. For the pelB construct, cells were disrupted by osmotic shock, resuspended in 30 mM Tris, pH 8.0, plus 20% sucrose, pelleted with centrifugation, resuspended in water (∼4 °C), stirred for 20 min, and repelleted. The two supernatants were combined, brought to 100% ammonium sulfate saturation, stirred on ice for 2 h, and centrifuged. The pellet was resuspended in 20 mM Tris, pH 8.0, dialyzed overnight against the same buffer plus 2 M ammonium sulfate, and purified over hydrophobic interaction (phenyl sepharose; Amersham Biosciences) and Superdex 75 (Amersham Biosciences) gel filtration columns. The protein concentration was calculated with an extinction coefficient of 21.3 mM^{-1} cm^{-1} at 278 nm (*18*). Metal analysis with inductively coupled plasma-mass spectrometry indicated that Ni was the only first row transition metal of significant concentration (0.4 Ni ions per subunit). SOD activity was measured qualitatively with a nitroblue tetrazolium native gel-based assay.

Crystallization, Diffraction Data Collection, and Refinement. NiSOD from the Met0 construct was crystallized at 13 mg/mL in the orthorhombic space group $C222_1$ (a = 60.43 Å, b = 110.24 Å, and c = 110.66 Å) by using the hanging drop method against 22% MPEG (Fluka) 2000, 50 mM Hepes, pH 8.0, 5% methanol, and 50 mM $CaCl_2$. This crystal form contains a solvent content of 47% and three subunits in the asymmetric unit. Phases were determined by a three wavelength MAD experiment conducted on the seleno-methionine protein (Table 1) performed at the European Synchrotron Radiation Facility (ESRF beamline BM14) using a CCD (MARUSA) detector. Six Se sites, corresponding to three copies each of Met28 and Leu85Met, were identified in SOLVE (*28*), refined in SHARP (*29*) with Solomon density modification (*30*), and used to calculate initial electron density maps of sufficient quality to trace the entire model except for 8−10 disordered N-terminal residues. The resulting trimeric NiSOD structure was refined against the 2.8 Å resolution diffraction data (Table 1) to a R_{work} of 23.5 (R_{free} of 29.2). Crystallographic 2-fold symmetry replicated this trimer, to generate a hexameric enzyme complex with clear solvent boundaries.

Native NiSOD crystals grew at 24 mg/mL from similar conditions to Met0 NiSOD but in the monoclinic space group $P2_1$ (a = 64.15 Å, b = 111.68 Å, and c = 106.83 Å, β =

94.51) with a solvent content of 48% and 12 molecules per asymmetric unit. Initial crystal clusters were crushed, serially diluted in a stabilizing solution (50 mM Hepes, pH 8.0, 50 mM $CaCl_2$, 5% methanol, and 15% MPEG 5000), and used as microseeds to grow large single crystals. Diffraction data were obtained at the Advanced Light Source (ALS beamline 8.2.2) using a 3 × 3 CCD detector. Phases were determined with the molecular replacement program AMoRe (*23*) using our previously built NiSOD trimer as a search model. The resulting structure, refined without noncrystallographic symmetry restraints to a R_{work} of 15.8 (R_{free} of 20.1), contains two hexameric NiSOD enzymes with excellent stereochemistry; all residues are in the additional allowed regions (96% in the most favored) of the Ramachandran plot. The very low B-factors for the nickel ions (Table 1) and excellent fit to electron density maps indicate full metal ion occupancy. The final structure includes 1397 residues, 12 Ni ions, and 1958 water molecules.

Cocrystallization of native NiSOD with cyanide resulted in the determination of the apo structure. NiSOD was cocrystallized with 20 mM cyanide at 24 mg/mL in the $C222_1$ space group (a = 60.04 Å, b = 112.49 Å, and c = 111.30 Å). Crystal quality was improved by microseeding techniques. The CN-treated data set was collected at the Advanced Light Source [SIBYLS (Structurally Integrated Biology for Life Sciences) beamline 12.3.1] using a 3 × 3 CCD detector. Phases were determined with AMoRe (*23*) using a trimer search model derived from the native NiSOD structure.

For diffraction data collection, crystals were cryocooled immediately after immersion in the stabilizing solution plus 20% ethylene glycol. All data sets were indexed and reduced with the HKL package (*20*). Difference electron density and omit maps were manually fit with the XtalView package (*21*) and refined in either CNS (*22*) or SHELX-97 (*24*) using all diffraction data, except for 5% used for R_{free} calculations (*25*). Structurally similar proteins were identified (*26*) with the DALI server (www2.ebi.ac.uk/dali; version 2.0). The coordinates have been deposited in the PDB under the PDB code 1T6I, 1T6Q, and 1T6U.

RESULTS

Active Recombinant NiSOD. To create active recombinant NiSOD, we reengineered the gene to remove the *S. coelicolor* leader sequence. In Met0 NiSOD, this leader sequence was replaced by a single methionine residue, whose presence was confirmed by mass spectrometry. However, Met0 NiSOD lacked the absorbance and EPR spectroscopic signatures characteristic of native source NiSOD and was inactive. In the pelB NiSOD construct, the replacement leader sequence from pelB was properly cleaved, leaving His1 as the mature N terminus. Recombinant NiSOD from this construct bound Ni, had SOD activity comparable to CuZnSOD on a gel-based assay, was redox active, and exhibited a resting state EPR spectrum matching that of NiSOD purified from the native source (Figure 1). Consistent with our results, a recombinant Factor Xa cleavage system recently was also shown to generate NiSOD with native properties (*27*). Thus, both biochemical and spectroscopic data indicate that recombinantly expressed NiSOD with the properly processed His1 N terminus reproduces the active site of native NiSOD,

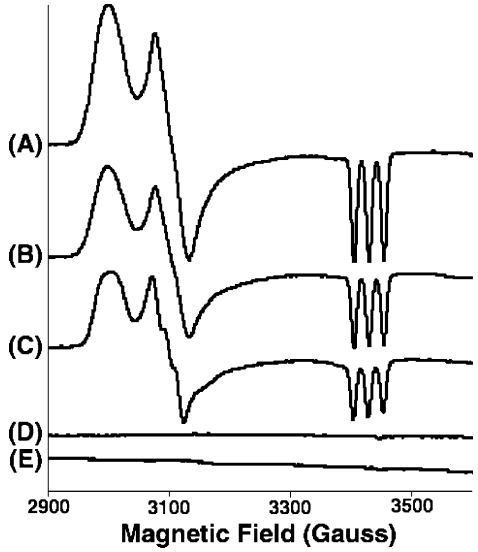

FIGURE 1: EPR spectra for recombinant *S. coelicolor* NiSOD in functional and inhibited states. EPR spectra displayed for (A) oxidized NiSOD (spin intensity of 0.72 spins/Ni); (B) as-isolated NiSOD (0.50 spins/Ni); (C) azide-treated (200 mM), oxidized NiSOD; (D) dithionite (10 mM)-reduced NiSOD; and (E) cyanide-treated (117 mM), oxidized NiSOD. NiSOD was prepared in 50 mM Hepes, pH 8.0. NiSOD concentrations were 777 μM for samples A, B, and D; 645 μM for sample B; and 683 μM for sample E. Samples were oxidized with 3.3 mM $K_3Fe(CN)_6$. As-isolated and oxidized samples exhibit g values of 2.30, 2.22, and 2.01, while the azide spectrum has a perturbed g_y = 2.24 feature. EPR spectra were collected at 55 K using a microwave frequency of 9.678 GHz, microwave power of 10 mW, and modulation amplitude of 5 G. The inhibitors were incubated for 2 h prior to freezing for EPR analysis.

whereas even a single additional N-terminal residue inhibits productive active site formation.

4-Helix Bundle Subunit Fold. The native NiSOD structure, determined to 1.30 Å resolution, revealed that the subunit fold is a right-handed 4-helix bundle with up−down−up−down topology (Figure 2A). In the 2.80 Å Met0 structure, the N-terminal 7−8 residues are disordered. In the native structure, these residues form a "hook" that protrudes from the 4-helix bundle to chelate the active site Ni ion. The subunit architecture contains two pairs of parallel helices, α2/α3 and α1/α4, with a short connecting helix (αC) between α2 and α3. The interhelical or crossing angle between nonparallel helices is 19°, which is commonly observed in 4-helix bundles and allows pairs of helices to remain in contact over a greater distance (*31*). Analysis by DALI (*26*) suggests that the subunit fold is structurally most similar to the 4-helix bundle of the cytoskeletal protein α-1 catenin (PDB code 1H6G; with a *Z*-score of 9.8 and RMSD of 2.5 Å), which functions in modulating cell adhesive strength. Metalloproteins cytochrome b562 (PDB code 256B; *Z*-score 8.1) and hemerythrin (PDB code 2MHR; *Z*-score 5.9) share similar folds but house their metal ions inside, rather than outside, their 4-helix bundles. Thus, NiSOD reveals a novel mode for metal binding by a 4-helix bundle fold.

The NiSOD subunit has extensive hydrophobic packing at the base of the 4-helix bundle from α2 (Val55, Leu58, and Trp59), α3 (Leu74, Leu77, and Val78), α4 (Ile104, Ile107, Ile110, Phe111, and Trp112), and the α2/αC loop (Phe63). Stabilization of the turns between helices is achieved

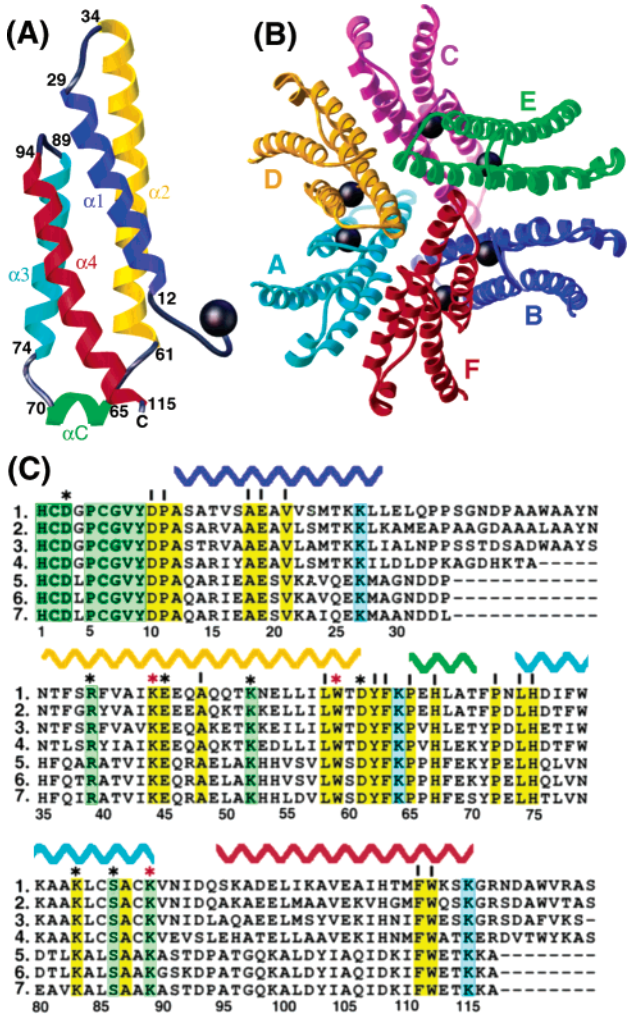

FIGURE 2: NiSOD subunit and hexameric structure. (A) NiSOD subunit with metal binding hook and residue labels for the ends of helices. (B) NiSOD biological unit is a hexameric assembly of 4-helix bundles. The 3-fold axes relate subunits A−C and D−F. Ni ions displayed in dark gray. (C) Conservation for identified NiSOD sequences. (1) *Prochlorococcus marinus* str. MIT 9313, (2) *Synechococcus* sp. WH 8102, (3) *Prochlorococcus marinus* MED4, (4) *Trichodesmium erythraeum* IMS101, (5) *Streptomyces avermitilis* MA-4680, (6) *S. coelicolor* A3(2), and (7) *S. seoulensis*. Numbering for *S. coelicolor*. (Leader sequences not shown.) Corresponding helices from panel A displayed above the sequence alignment. Residues that contribute to subunit stability (I), hexamer stability (∗), or both (red ∗) are marked. Conserved residues that contribute to the Ni-hook or its stabilization are shown in green. Conserved electrostatic residues are shown in blue, and other conserved residues are shown in yellow.

by hydrogen bonds from Asn31, Asp33, and Gln37 side chains to peptide backbone atoms of the α1/α2 turn and similar interactions from Gln25, Lys44, Asp93, and Thr96 to the α3/α4 turn. Interhelical interactions further stabilize each subunit: salt bridges between Glu17-Arg47 and Glu49-Lys89 pairs plus hydrogen bonds between Lys22-Gln98 and Trp59-His75. Surprisingly, the exterior surface of each NiSOD subunit contains almost exclusively polar and charged side chains with no obvious major hydrophobic face for multimeric assembly.

Hexameric Assembly. Our structures indicate, however, that the NiSOD biological unit is a hexameric assembly of 4-helix bundles (labeled A−F). Sets of three subunits (A, B, and C; D, E, and F) come together like the legs of a tripod about a 3-fold axis (Figure 2B), through contacts of the N-terminal ends of their α2 helices. Salt bridge (Arg39A-Glu45C, Arg39B-Glu45A, and Arg39C-Glu45B), hydrophobic (Val42A with Val42B and Val42C), and water-mediated hydrogen bond (Gln46A with Gln46B and Gln46C) interactions fortify these trimers. The N and C termini and the short connecting helix (αC) of each subunit form the "feet" of the tripods. Top and bottom trimers, related by 2-fold axes perpendicular to the 3-fold, interlock their legs to form the hexamer. This architecture places each Ni-binding active site hook into a slot created between two 4-helix bundles of the opposing trimer at the 3-fold axis (Figure 2B). The hexamer is primarily stabilized across this 2-fold axis by hydrophobic (Trp59A with Trp59F), salt bridge (Lys52A-Asp61F, Lys52A-Asp3F, and Lys89A-Asp3F), and hydrogen bond (Ser56A with Ser56F, His75A with Gln76F, and Gln76A with His75F) interactions. Furthermore, Lys83F satisfies hydrogen bonds for backbone atoms of an adjacent α2/αC loop.

Hexameric NiSOD is roughly spherical and hollow, with an outside diameter of 60 Å and a large interior cavity [8758 Å^3 volume calculated (*32*) at the molecular surface] 20 Å in diameter. The enzyme assembly is remarkably similar, albeit smaller, to those of the DNA binding and protection protein Dps (12 4-helix bundles in 87 Å diameter sphere with a 45 Å diameter core) and the iron storage protein ferritin (24 4-helix bundles in 130 Å diameter sphere with a 75 Å diameter core). In these proteins, iron is stored inside the central cavity. In our NiSOD structure, the six nickel ions are arranged in an octahedral geometry about an empty cavity. The catalytic metal sites within the NiSOD hexamer do not interact. The closest pairs of Ni ions lie 23 Å apart across the 2-fold axes between trimers and the farthest, octahedrally opposing, pairs are separated by 35 Å.

Sequence Conservation, Electrostatic Guidance, and the Active Site Channel. To understand structure−function relationships in NiSOD, we searched for all family members and analyzed their sequence conservation. In contrast to the other ubiquitous SODs, NiSOD appears to be limited to the soil bacteria *Streptomyces* and the cyanobacteria. Nickel is abundant in the ecological niches of these aerobes: Ni concentrations are similar to those of Cu and Zn in soil (*33*) and equivalent to or higher than Cu, Fe, or Mn concentrations (*34*) in seawater. Sequence conservation among the seven NiSODs (Figure 2C) is concentrated in the nine-residue N-terminal Ni-hook motif and key residues contributing to the hydrophobic core of the 4-helix bundle and the hexameric assembly of these subunits. Sequence insertions are observed only in the α1/α2 loop and the C terminus of the cyanobacterial NiSODs, where they are unlikely to significantly perturb the subunit fold or hexameric structure.

Besides the residues contributing to the Ni site, enzyme fold, and assembly, structural analysis furthermore identifies three conspicuously conserved lysine residues (Figure 2C) that form an electrostatic guidance system to the active site, like those found in other SODs. Conserved lysines Lys64 and Lys115, together with Lys27D from the 2-fold related subunit, form a triangle with a positive electrostatic potential surface 10−12 Å out from the active site nickel ion (Figure 3). Roughly perpendicular to the lysine triangle, the Ni-hook forms a ledge at the base of a 15 Å wall, constructed from the α3 and α4 helices of a third subunit (F, Figure 3B,D). A narrow active site channel, approximately 7 Å deep, limits

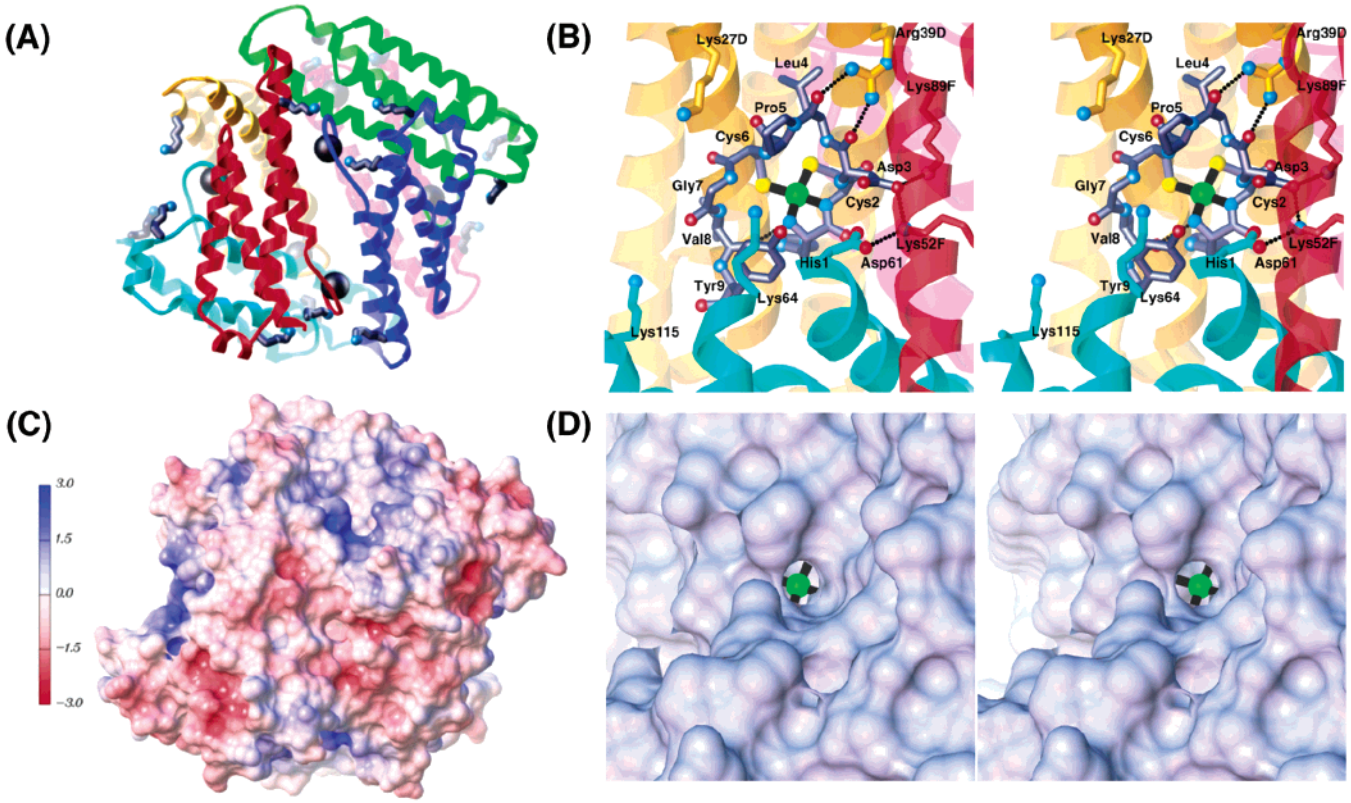

FIGURE 3: NiSOD electrostatic potential, active site channel, and Ni-hook. (A) Overall hexamer fold displayed as a ribbon diagram rotated roughly 90° from that in Figure 2B showing conserved lysine residues Lys64, Lys115, and Lys27 for each subunit. Subunits related by 2-fold axes are displayed in red/blue, green/purple, and yellow/cyan. (B) Stereoview showing the active site and Ni-hook geometry for the cyan subunit, displayed in a view similar to panel A. (C) The electrostatic potential grid was calculated with UHBD (*49*), and the molecular surfaces were calculated with MSMS (*50*) using a 1.4 Å probe radius. (D) Stereoview for the active site channel displayed as a van der Waals surface. The electrostatic potential at the solvent accessible surface was then mapped back onto the molecular surface and displayed in red (negative) and blue (positive). Units are in kcal mol^{-1} e^{-1}. The six electropositive triangles of lysine residues are distributed octahedrally on the surface of the hexamer.

access to the open axial coordination position of the Ni ion. The top of this channel lies between Lys64 and a trio of conserved residues (Lys83F, Ser86F, and Ala87F) from the α3F wall. The channel is further constricted by the side chain of hook residues Pro5 and Tyr9 (located beneath Lys64) and the carboxylate of Asp61, which begins a chain of salt bridges (Asp61A to Lys52F to Asp3A to Lys89F) underlying the α3F wall. The active site channel narrows at the base to under 3 Å, less than the van der Waals diameter of an oxygen atom (3.04 Å).

N-Terminal Ni-Hook and the Active Site. The Ni-hook motif exhibits an unusual conformation reminiscent of a macrocyclic host molecule (Figure 3B). The backbone nitrogen atoms of residues 1−8 (excluding Pro5) are all directed inward with the carbonyl oxygen atoms pointed outward. Notably, Pro5 exhibits a cis-peptide bond conformation. The macrocyclic hook conformation is stabilized by residues from two adjacent subunits (D and F) of the opposing trimer. Salt bridges link the Asp3 side chain to Lys89F and Lys52F. The carbonyl oxygen atoms of Asp3 and Leu4 form hydrogen bonds to Arg39D, and the carbonyl of Val8 closes the macrocycle with a hydrogen bond to the N-terminal nitrogen atom. The other carbonyl groups of the Ni-hook, His1, Cys2, Pro5, Cys6, and Gly7, interact exclusively with water molecules.

Both oxidized (Ni^{3+}) and reduced (Ni^{2+}) functional states were revealed in electron density maps (Figure 4A) for our 1.30 Å resolution diffraction data set (Table 1). The high resolution permitted crystallographic refinement of both metal sites without restraints that could bias metal site geometry (Table 2). The most striking feature of the active site is the dual conformations for His1. In one conformation, the His1 side chain is not a Ni ligand but forms hydrogen bonds to Glu17D and the backbone carbonyl of Val8, suggesting a positively charged side chain (Figure 4B). The Ni ion binds to the N-terminal amine of His1, the backbone amide of Cys2, and the thiolates of Cys2 and Cys6 in a square planar geometry. In the second conformation, the His1 ring becomes an axial Ni ligand, making a five coordinate square pyramidal site (Figure 4C). The electron density for His1 also reveals multiple positions for the Cβ and backbone nitrogen (but not Cα or carbonyl) atoms, correlating with the dual side chain conformations (Figure 4A). Refinement of His1 side chain occupancies indicates an equal mixture of the two conformations (43−57% each) that correlates well with the observed EPR spin intensity (Figure 1) and defines a His1 φ torsion and side chain coordination change between oxidized and reduced states.

Inhibitors/Inactivators of NiSOD. To characterize mechanisms for NiSOD inhibition by anionic inhibitors, we examined the interaction with azide and cyanide. NiSOD activity is lowered 50% by 42 mM azide (*17*) and abolished by 10 mM cyanide (*14*). We discovered that treating NiSOD with 200 mM ^{14}N-azide (nuclear spin I = 1) alters the EPR spectral properties by shifting and introducing hyperfine splitting in the g_y tensor (Figure 1C). NiSOD treated with

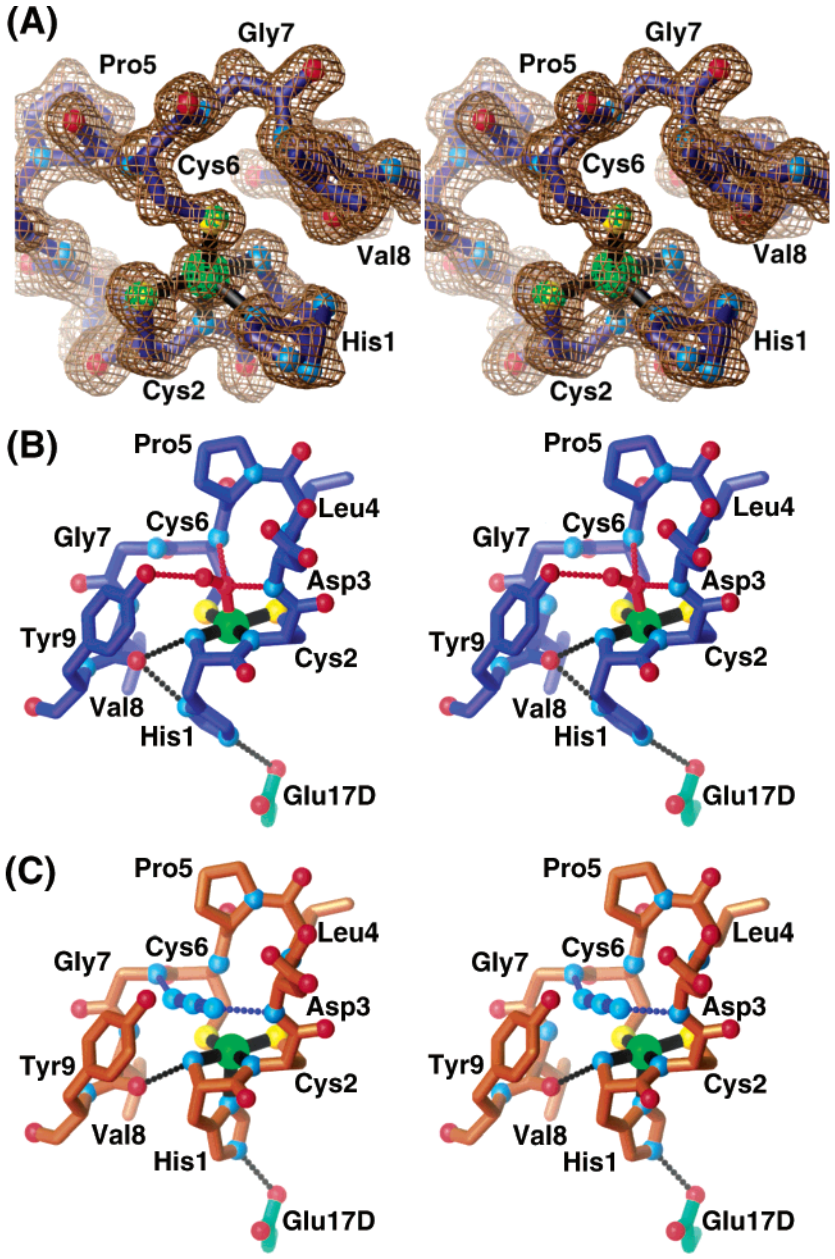

FIGURE 4: Stereoviews of NiSOD active site hook and coordination geometry. (A) Oxidized and reduced functional states of NiSOD with $2F_o - F_c$ electron density contoured at 1 (brown) and 10 (green) σ. (B) Square planar geometry displayed for Ni^{2+} state. The modeled superoxide (red) is shown ligated to the Ni ion. (C) Square pyramidal geometry shown for Ni^{3+} species. The modeled azide (blue) is displayed spanning the Ni-hook macrocycle.

^{15}N-labeled azide ($I = 1/2$) reproduces this altered spectra, indicating that the hyperfine interactions result from structural/electronic perturbations, rather than azide ligation to the nickel ion. In contrast, cyanide treatment of NiSOD results in complete loss of EPR active species (Figure 1E), even in the presence of oxidant. Although this loss could result from conversion of EPR active Ni^{3+} to EPR silent Ni^{2+}, cyanide binding would be expected to induce the opposite trend (*35*). Determination of a 2.05 Å resolution cocrystal structure for CN-treated NiSOD (Table 1) revealed an alternative mode for cyanide inhibition: nickel removal by cyanide chelation. Although CN-treated NiSOD has a properly processed N terminus, its structure matches that of Met0 NiSOD: the Ni-hook is disordered, and there is no evidence for Ni binding. This result argues that Ni ion binding is needed to order the N-terminal Ni-hook. In contrast, metalloenzymes active sites are typically preordered within the protein environment; the metal ligands often distort the metal site geometry to enhance catalysis [entatic state hypothesis (*36*)].

DISCUSSION

NiSOD Maturation. Analysis of our structural and functional results, together with previous biochemical data (*37*), supports a specific Ni-regulated model for NiSOD maturation consisting of three sequential steps: hexamer assembly, Ni-activated proteolytic cleavage, and Ni-hook formation (Figure 5). The Met0 and CN-treated apo structures demonstrate that hexameric assembly occurs in the absence of Ni and can precede proteolytic cleavage of the leader sequence. From the unfolded N terminus in our Met0 structure, we infer that even one extra N-terminal residue blocks Ni-hook formation, consistent with our Ni-bound structure, in which Tyr9

Table 2: NiSOD Bond Lengths and Angles

Bond Lengths (Å)

	NiSOD[a]	([Ni(ema)]$^{2-}$)[b]	EXAFS[c]	CSD[d]	MDB[e]
$Ni^{2+/3+}$−Cys2 SG	2.16 ± 0.02	2.179	2.160(4)	2.24 ± 0.12	2.30 ± 0.12
$Ni^{2+/3+}$−Cys6 SG	2.19 ± 0.02	2.179	2.160(4)	2.24 ± 0.12	2.30 ± 0.12
$Ni^{2+/3+}$−Cys2 N	1.91 ± 0.03	1.858	1.91(1)	1.93 ± 0.11	
Ni^{2+}−His1 N	1.87 ± 0.06	1.858	1.91(1)	2.04 ± 0.11	
Ni^{3+}−His1 N	2.02 ± 0.10			2.04 ± 0.11	
Ni^{3+}−His1 ND1	2.35 ± 0.05			2.09 ± 0.05	2.15 ± 0.18

Bond Angles (°)

	NiSOD[a]	([Ni(ema)]$^{2-}$)[b]
Cys2 N−Ni^{2+}−His1 N	83.6 ± 1.6	85.6
Cys6 SG−Ni^{2+}−His1 N	93.3 ± 1.3	88.4
Cys2 SG−$Ni^{2+/3+}$−Cys6 SG	95.0 ± 0.6	97.4
Cys2 SG−$Ni^{2+/3+}$−Cys2 N	88.2 ± 0.7	88.4
Cys2 N−Ni^{3+}−His1 N	81.5 ± 1.4	
Cys6 SG−Ni^{3+}−His1 N	95.8 ± 1.1	
His1 ND1−Ni^{3+}−His1 N	81.5 ± 1.6	
His1 ND1−Ni^{3+}−Cys2 N	82.3 ± 1.5	
His1 ND1−Ni^{3+}−Cys2 SG	106.7 ± 1.5	
His1 ND1−Ni^{3+}−Cys6 SG	94.4 ± 1.6	

[a] Standard deviation errors for the 12 NiSOD subunits in monoclinic crystal form. [b] From Kruger et al. (*43*). [c] EXAFS fit RE4 (*17*). [d] Standard deviation errors for Ni−thiolate (N_{obs} = 5426), Ni−imidazole (N_{obs} = 188), Ni−amine (N_{obs} = 19 447), and Ni−amide (N_{obs} = 298). [e] Standard deviation errors for metal−thiolate (N_{obs} = 7630) and metal−imidazole (N_{obs} = 3072).

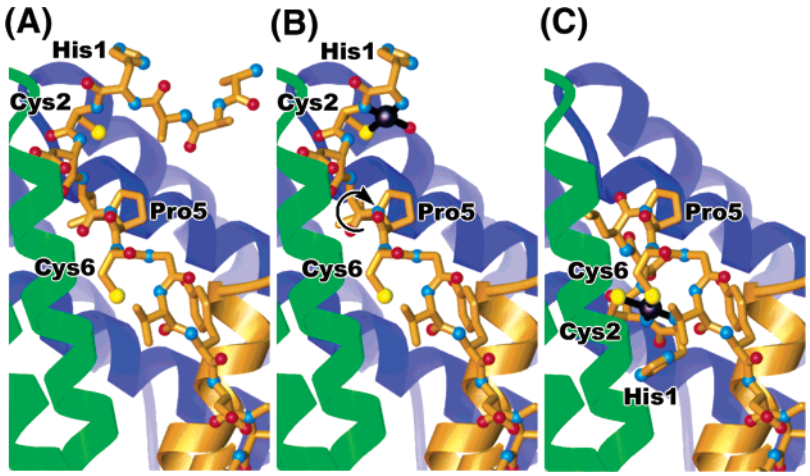

FIGURE 5: NiSOD maturation model. (A) Hexamer assembly with modeled trans peptide for Pro5 that extends the N-terminal residues and leader sequence for processing. (B) Ni-activated proteolytic cleavage. (C) Ni-hook formation by trans-to-cis isomerization and Cys6 ligation.

sterically precludes residues N-terminal to His1. Moreover, the observed ~15° φ torsion for His1 between the reduced and the oxidized states of NiSOD produces movements of the His1 backbone nitrogen that would otherwise be energetically prohibited by the constraints of the preceding peptide bond. We therefore propose that the NiSOD leader sequence is a prosequence rather than a targeting sequence. This is consistent with the NiSOD cytosolic location (*14*). Thus, the NiSOD leader sequence maintains the proenzyme in an inactive conformation prior to the proteolytic cleavage required for enzyme maturation (*14*), by a mechanism similar to that of Ni hydrogenases and many protease zymogens. For NiSOD, cleavage of this prosequence frees the His1 N terminus for Ni binding and for conformational changes required in redox cycling.

During NiSOD maturation, Ni binding and proteolytic cleavage are likely coupled (Figure 5). The Ni-bound structure reveals that all Ni ligands are found within the six-residue sequence immediately following the cleavage site. Ni also ligates the nitrogen atom freed by proteolytic cleavage. Furthermore, the ratio of cleaved to uncleaved NiSOD was shown to be increased by added nickel, whereas Ni chelators abolished proteolytic maturation (*37*). Similarly, Ni activates proteolytic maturation in Ni−Fe hydrogenase (*38*). Ni binding to the hydrogenase large subunit, rather than to the HycI protease, provides the trigger.

Trans-to-cis isomerization of Pro5 is required for maturation of the Ni-hook motif. With Pro5 in trans, His1 and Cys2 can still provide three of the four square planar Ni^{2+} ligands, but Cys6 is misaligned. Moreover, the residues N-terminal to Pro5 are extended outside of the hexamer, exposing the leader sequence for processing (Figure 5A). We postulate that chelation of Ni^{2+} by His1 and Cys2 promotes proteolytic maturation. When Pro5 then is trans-to-cis isomerized, binding of Cys6 to Ni^{2+} completes the square plane, locks Pro5 into the mature cis-peptide conformation, and forms the mature Ni-hook motif (Figure 5). In the apo structures, residues stabilizing the Ni-hook motif from the outside (Arg39, Lys52, and Lys89) are preorganized by additional interactions that maintain their conformation in the native

Ni-bound hexamer.

Channel to Active Site. SODs are so-called "perfect" enzymes, exhibiting rapid diffusion-limited catalytic rates, enhanced by electrostatic guidance for the anionic superoxide substrate to the catalytic site (*39*). NiSOD is no exception. Although the overall net negative charge of NiSOD (est. −12 at pH 8.0) would repel superoxide anion, three conserved Lys residues are positioned near the active site channel to attract the anionic substrate, consistent with the decrease in k_{cat} at higher ionic strength (*17*). All SOD classes exhibit electrostatic guidance and possess attractive surface lysine residues 9−13 Å from the catalytic metal ion. Likewise, all active site channels are constricted to about the diameter of an oxygen atom, so as to desolvate superoxide and limit access of larger nonphysiological substrates to the active site. The NiSOD channel is more similar to that of FeSOD/MnSOD than CuZnSOD. The NiSOD channel shares with the FeSOD/MnSOD funnel similar widths, multisubunit assemblies, and gateway tyrosine residues that cap the active site metal ions. Brownian dynamics simulations indicate that omission of MnSOD Tyr34 allows access of substrate to the metal, suggesting that this residue may move to allow metal ligation (*40*). Similarly, the NiSOD Tyr9 is positioned to constrict the active channel, gating substrate access to the nickel ion. Thus, the electrostatic guidance and restrictive channel access characterized for other SODs has also evolved in NiSOD, supporting the biological importance of electrostatic interactions for SOD functions in reactive oxygen defense.

Metal Site Geometry and Tuning of Reduction Potential. The reduced NiSOD active site exhibits undistorted, four-coordinate, square planar Ni^{2+} geometry, unlike the previously proposed (*17*) dinuclear Ni site. Ni^{2+} and its ligands lie within 0.1 Å of their least squares plane, and ligand−metal−ligand angles are near 90° (Table 2). Ni−S (2.17 ± 0.02 Å) and Ni−N (1.89 ± 0.05 Å) bond lengths are self-consistent among the 12 NiSOD active sites (Table 2). The Ni−S bond lengths are slightly shorter than Ni−thiolate bonds in the Cambridge Structural Database (CSD) (*41*) and metal−thiolate bonds in the Metalloprotein Database and Browser (MDB) (*42*) and significantly shorter than the limited number of Ni to protonated thiol bonds in the CSD (2.46 ± 0.14 Å, $N_{obs} = 5$). The Ni−N bond lengths to the doubly protonated N-terminal amine and deprotonated Cys2 amide are similar to those of Ni−amino and Ni−amido complexes in the CSD. The square planar geometry of the reduced NiSOD site matches that proposed from X-ray absorption near edge structure (XANES) spectroscopy (*17*) and that determined for the $[Ni(ema)]^{2-}$ model compound (*43*) with two thiolate and two amidate ligands. The Ni−S and Ni−N bond lengths of reduced NiSOD are strikingly similar to those from this $[Ni(ema)]^{2-}$ model compound and from the NiSOD EXAFS model with correct (2N, 2S) ligation (Table 2), which was surprisingly assigned a worse goodness of fit than the incorrect dinuclear model (*17*).

Addition of an axial histidine ligand to the oxidized NiSOD active site creates Ni^{3+} square pyramidal geometry and tunes the reduction potential for superoxide dismutation. The axial His1 ND1 ligand exhibits a much longer bond length to Ni^{3+} than typical Ni−imidazole molecules in the CSD or metalloproteins in the MDB (Table 2). This axial His ND1 ligand explains the EPR three-line hyperfine

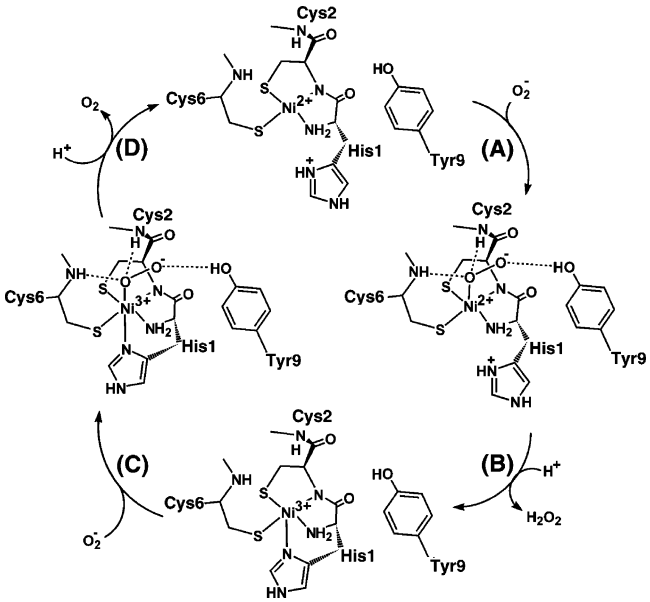

FIGURE 6: NiSOD catalytic mechanism.

splitting pattern (Figure 1A) characteristic of ^{14}N (nuclear spin I = 1) interactions with an unpaired electron in the dz^2 orbital. Binding the axial His1 imidazole ligand and switching from square planar to square pyramidal geometry would increase ligand field stabilization, thus favoring Ni^{3+} and lowering the midpoint potential of the $Ni^{3+/2+}$ couple (often in excess of 1 V) into the range suitable for superoxide dismutation [−0.16 to 0.89 V vs NHE (*44*)]. Activity and EPR spectroscopic data on the His1Gln NiSOD variant (*27*) support the role of the axial ligand in redox tuning. Similar hyperfine features for the wild-type and His1Gln mutant NiSODs suggest that the Gln side chain nitrogen substitutes as the axial ligand. The resting state EPR spin intensity for this mutant indicates a higher than wild-type redox potential, which is coupled to lower, but significant, activity (*27*). In contrast, the distal Ni^{2+} site of acetyl-CoA synthase is likely redox inactive during catalysis, as proposed by Darnault et al. (*45*), because it lacks an axial ligand, although it shares with reduced NiSOD square planar ligation by two Cys side chains and two backbone nitrogen atoms (*45*, *46*).

Proposed Mechanism. On the basis of the metal ligand geometry and active channel topography of NiSOD, superoxide binds to the open axial Ni coordination site at the base of the channel, opposite to the His1 side chain. In our docked superoxide model (Figures 4B and 6), the Ni-bound oxygen atom is within hydrogen-bonding distance and properly oriented to interact with the backbone nitrogen atoms of Asp3 and Cys6, and the nonligating oxygen atom is in hydrogen-bonding distance to Tyr9. This model supports electron transfer between the superoxide substrate and the active site Ni ion through inner sphere mechanisms. Linear triatomic azide, unlike diatomic superoxide, collides with Tyr9 or backbone amides, when modeled as a nickel ligand. Azide can be modeled to span the Ni-hook macrocycle between the Asp3 and the Gly7 amide nitrogen atoms (Figure 4C), 3.1 Å from the Ni ion. EPR spectroscopy confirms that azide binds near, but not to, the Ni^{3+} ion (Figure 1C).

Electron transfer from the Ni^{2+} catalyst to superoxide must be coupled to proton transfer to generate the hydrogen peroxide product (Figure 6B). At first, one might attempt to

correlate the proton-donating catalytic role of the bridging histidine in CuZnSOD with the axial His1 ligand of NiSOD; both imidazoles only bind the metal ion in the oxidized state and lose protons upon metal binding. However, His1 is located on the wrong side of the nickel ion, opposite from the substrate-binding site. Alternatively, a protonated thiol has been suggested as the proton donor during superoxide reduction to hydrogen peroxide (*17*). The short Ni−thiolate bond lengths and lack of stabilizing proton acceptors contradict this hypothesis. Instead, we propose that the properly positioned backbone amides of Asp3 or Cys6 or the side chain hydroxyl of Tyr9 can donate protons for hydrogen peroxide formation (Figure 6B). As a proton donor, NiSOD Tyr9 is analogous to MnSOD Tyr34, which is also located 5 Å from its catalytic metal ion and similarly oriented (*47*). Following conformational changes in NiSOD His1, to convert from four-coordinate square planar to five-coordinate square pyramidal geometry upon Ni oxidation, superoxide again binds axially to the Ni ion (Figure 6C), and electron transfer reduces Ni^{3+} to Ni^{2+} and generates molecular oxygen to complete the catalytic cycle (Figure 6D).

Ni-Hook Sequence Motif. The Ni-hook motif by itself generates almost all functionally critical interactions for NiSOD activity. The active site Ni ion ligands are all contained in the Ni-hook motif as are the substrate stabilizing (Ni-hook backbone amides and Tyr9), channel constricting (Pro5 and Tyr9), and hinge (Pro5) residues. In *S. coelicolor* NiSOD, although Asp3 stabilizes the Ni-hook and Val8 blocks backside access to the Ni ion, neither interaction is amino acid specific. Thus, we propose that the Ni-hook motif, N-terminal His-Cys-X-X-Pro-Cys-Gly-X-Tyr, will be diagnostic of NiSODs. In fact, searching protein databases with this motif, we predict that the 156 amino acid hypothetical protein (CAD77695) from the marine planctomycete *Pirellula* sp. strain 1, which shows only 21% overall sequence identity, is a NiSOD.

Conserved Structure−Function Relationships among SOD Families. The absence of sequence and structure similarity of NiSOD with CuZnSOD or Mn/FeSOD demonstrates independent evolution, emphasizes the importance of SOD for aerobic environments, and helps elucidate essential structure−function relationships. SODs must mediate both oxidation and reduction of superoxide, implying a range of midpoint potentials (between −0.16 and 0.89 V vs NHE) that can support activity. To afford maximum thermodynamic driving force, each class of SOD uses a different mechanism to tune their midpoint potential near the middle of this range: CuZnSOD at 0.4 V, FeSOD at 0.26 V, and MnSOD at 0.31 V near pH 7.0 (*44*). For Fe/MnSODs, the Fe and Mn ions utilize the same ligand sets in nearly identical active sites; yet, substitution of Mn into FeSOD or Fe into MnSOD leads to inactive enzyme due to opposing shifts in midpoint potential by the two protein environments (*48*). In CuZnSOD, the polypeptide imposes a "Cu rack", distorting the preferred Cu^{2+} tetrahedral geometry toward the Cu^{1+} trigonal plane. In contrast, the Ni-hook of NiSOD binds Ni with little geometric distortion (Table 2) and is unstructured in the absence of metal ion, like Zn finger proteins but unlike most metalloenzyme active sites. Instead, NiSOD binds an axial ligand to tune the reduction potential. Thus, for each class of SOD, a distinct protein sequence, structure, and assembly invokes a different mechanism to appropriately tune the coordination chemistry of its own metal ion for superoxide dismutation. Our analyses and comparisons of NiSOD structure−function relationships with those of other SOD families identify six conserved features: electrostatic guidance, a sterically restricted active site channel, an open coordination site for direct superoxide binding, hydrogen bonding to bound superoxide, suitable enzyme environments for oxidized and reduced metal ion geometries, and metal ions poised at appropriate reduction potentials.

ACKNOWLEDGMENT

We thank C. D. Putnam, L. Noodleman, P. A. Lindahl, D. B. Goodin, and T. I. Wood for scientific discussions, D. B. Goodin for assistance with EPR spectroscopy, S. J. Rigby and J. L. Huffman for metal analysis, B. R. Chapados and E. D. Garcin for MAD data collection at ESRF, and J. L. Huffman and J. J. Plecs for data collection at the ALS SIBYLS beamline.

REFERENCES

1. McCord, J. M., and Fridovich, I. (1969) Superoxide dismutase an enzymic function for erythrocuprein (hemocuprein). *J. Biol. Chem. 244*, 6049.
2. McCord, J. M., Keele, B. B., and Fridovich, I. (1971) Enzyme-based theory of obligate anaerobiosis−physiological function of superoxide dismutase. *Proc. Natl. Acad. Sci. U.S.A. 68*, 1024.
3. Winterbourn, C. C. (1993) Superoxide as an intracellular radical sink. *Free Radical Biol. Med. 14*, 85−90.
4. Halliwell, B. (1995) *Active Oxygen in Biochemistry*, Blackie Academic and Professional, New York.
5. Beyer, W., Imlay, J., and Fridovich, I. (1991) Superoxide dismutases. *Prog. Nucleic Acid Res. Mol. Biol. 40*, 221−253.
6. Wallace, D. C. (1992) Mitochondrial genetics: a paradigm for aging and degenerative diseases? *Science 256*, 628−632.
7. Tainer, J. A., Getzoff, E. D., Richardson, J. S., and Richardson, D. C. (1983) Structure and mechanism of copper, zinc superoxide dismutase. *Nature 306*, 284−287.
8. Rosen, D. R., Siddique, T., Patterson, D., Figlewicz, D. A., Sapp, P., Hentati, A., Donaldson, D., Goto, J., O'Regan, J. P., Deng, H. X., and et al. (1993) Mutations in Cu/Zn superoxide dismutase gene are associated with familial amyotrophic lateral sclerosis. *Nature 362*, 59−62.
9. Stallings, W. C., Powers, T. B., Pattridge, K. A., Fee, J. A., and Ludwig, M. L. (1983) Iron Superoxide-dismutase from Escherichia coli at 3.1-a resolution−a structure unlike that of copper−zinc protein at both monomer and dimer levels. *Proc. Natl. Acad. Sci. U.S.A.: Biol. Sci. 80*, 3884−3888.
10. Stallings, W. C., Pattridge, K. A., Strong, R. K., and Ludwig, M. L. (1985) The structure of manganese superoxide-dismutase from thermus-thermophilus-Hb8 at 2.4-a resolution. *J. Biol. Chem. 260*, 6424−6432.
11. Ringe, D., Petsko, G. A., Yamakura, F., Suzuki, K., and Ohmori, D. (1983) Structure of iron superoxide-dismutase from Pseudomonas ovalis at 2.9-a Resolution. *Proc. Natl. Acad. Sci. U.S.A.: Biol. Sci. 80*, 3879−3883.
12. Borgstahl, G. E., Parge, H. E., Hickey, M. J., Beyer, W. F., Jr., Hallewell, R. A., and Tainer, J. A. (1992) The structure of human mitochondrial manganese superoxide dismutase reveals a novel tetrameric interface of two 4-helix bundles. *Cell 71*, 107−118.
13. Touati, D. (1992) in *Molecular Biology of Free Radical Scavenging Systems* (Scandalios, J. G., Ed.) pp 231−261, Cold Spring Harbor Laboratory Press, Cold Spring Harbor, NY.
14. Youn, H. D., Kim, E. J., Roe, J. H., Hah, Y. C., and Kang, S. O. (1996) A novel nickel-containing superoxide dismutase from Streptomyces spp. *Biochem. J. 318* (Pt. 3), 889−896.
15. Youn, H. D., Youn, H., Lee, J. W., Yim, Y. I., Lee, J. K., Hah, Y. C., and Kang, S. O. (1996) Unique isozymes of superoxide dismutase in Streptomyces griseus. *Arch. Biochem. Biophys. 334*, 341−348.
16. Palenik, B., Brahamsha, B., Larimer, F. W., Land, M., Hauser, L., Chain, P., Lamerdin, J., Regala, W., Allen, E. E., McCarren, J., Paulsen, I., Dufresne, A., Partensky, F., Webb, E. A., and

Waterbury, J. (2003) The genome of a motile marine Synechococcus. *Nature 424*, 1037−1042.
17. Choudhury, S. B., Lee, J. W., Davidson, G., Yim, Y. I., Bose, K., Sharma, M. L., Kang, S. O., Cabelli, D. E., and Maroney, M. J. (1999) Examination of the nickel site structure and reaction mechanism in Streptomyces seoulensis superoxide dismutase. *Biochemistry 38*, 3744−3752.
18. Kim, F. J., Kim, H. P., Hah, Y. C., and Roe, J. H. (1996) Differential expression of superoxide dismutases containing Ni and Fe/Zn in Streptomyces coelicolor. *Eur. J. Biochem. 241*, 178−185.
19. Bentley, S. D., Chater, K. F., Cerdeno-Tarraga, A. M., Challis, G. L., Thomson, N. R., James, K. D., Harris, D. E., Quail, M. A., Kieser, H., Harper, D., Bateman, A., Brown, S., Chandra, G., Chen, C. W., Collins, M., Cronin, A., Fraser, A., Goble, A., Hidalgo, J., Hornsby, T., Howarth, S., Huang, C. H., Kieser, T., Larke, L., Murphy, L., Oliver, K., O'Neil, S., Rabbinowitsch, E., Rajandream, M. A., Rutherford, K., Rutter, S., Seeger, K., Saunders, D., Sharp, S., Squares, R., Squares, S., Taylor, K., Warren, T., Wietzorrek, A., Woodward, J., Barrell, B. G., Parkhill, J., and Hopwood, D. A. (2002) Complete genome sequence of the model actinomycete Streptomyces coelicolor A3(2). *Nature 417*, 141−147.
20. Otwinowski, Z., and Minor, W. (1997) Processing of X-ray diffraction data collected in oscillation mode. *Macromol. Crystallogr. A 276*, 307−326.
21. McRee, D. E. (1999) XtalView/Xfit a versatile program for manipulating atomic coordinates and electron density. *J. Struct. Biol. 125*, 156−165.
22. Brunger, A. T., Adams, P. D., Clore, G. M., DeLano, W. L., Gros, P., Grosse-Kunstleve, R. W., Jiang, J.-S., Kuszewski, J., Nilges, N., Pannu, N. S., Read, R. J., Rice, L. M., Simonson, T., and Warren, G. L. (1998) Crystallographic and NMR system (CNS): a new software system for macromolecular structure determination. *Acta Crystallogr. D 54*, 905−921.
23. Navaza, J. (1994) AMoRe: an automated package for molecular replacement. *Acta Crystallogr. A50*, 157−163.
24. Sheldrick, G. M., and Schneider, T. R. (1997) *Methods Enzymol. 277*, 319−343.
25. Brunger, A. T. (1992) The free *R* value: a novel statistical quantity for assessing the accuracy of crystal structures. *Nature 355*, 472−474.
26. Holm, L., and Sander, C. (1993) Protein-structure comparison by alignment of distance matrices. *J. Mol. Biol. 233*, 123−138.
27. Bryngelson, P. A., Arobo, S. E., Pinkham, J. L., Cabelli, D. E., and Maroney, M. J. (2004) Expression, reconstitution, and mutation of recombinant Streptomyces coelicolor NiSOD. *J. Am. Chem. Soc. 126*, 460−461.
28. Terwilliger, T. C., and Berendzen, J. (1999) Automated MAD and MIR structure solution. *Acta Crystallogr. D: Biol. Crystallogr. 55* (Pt. 4), 849−861.
29. La Fortelle, E. D., and Bricogne, G. (1997) Maximum-likelihood heavy-atom parameter refinement for multiple isomorphous replacement and multiwavelength anomalous diffraction methods. *Macromol. Crystallogr. A 276*, 472−494.
30. Abrahams, J. P., and Leslie, A. W. G. (1996) *Acta Crystallogr. D: Biol. Crystallogr. 52*, 30−42.
31. Kamtekar, S., and Hecht, M. H. (1995) Protein motifs. 7. The four-helix bundle: what determines a fold? *FASEB J. 9*, 1013−1022.
32. Liang, J., Edelsbrunner, H., Fu, P., Sudhakar, P. V., and Subramaniam, S. (1998) Analytical shape computation of macromolecules: II. Inaccessible cavities in proteins. *Proteins 33*, 18−29.
33. Andrews, R. K., Blakeley, R. L., and Zerner, B. (1988) in *Metal Ions in Biological Systems* (Sigel, H., Ed.) pp 165−284, Marcel Dekker, New York.
34. Mason, B., and Moore, C. B. (1982) *Principles of Geochemistry*, 4th ed., Wiley, New York.
35. Shearer, J., Fitch, S. B., Kaminsky, W., Benedict, J., Scarrow, R. C., and Kovacs, J. A. (2003) How does cyanide inhibit superoxide reductase? Insight from synthetic FeIIIN4S model complexes. *Proc. Natl. Acad. Sci. U.S.A. 100*, 3671−3676.
36. Vallee, B. L., and Williams, R. J. (1968) Metalloenzymes: the entatic nature of their active sites. *Proc. Natl. Acad. Sci. U.S.A. 59*, 498−505.
37. Kim, E. J., Chung, H. J., Suh, B., Hah, Y. C., and Roe, J. H. (1998) Transcriptional and posttranscriptional regulation by nickel of sodN gene encoding nickel-containing superoxide dismutase from Streptomyces coelicolor Muller. *Mol. Microbiol. 27*, 187−195.
38. Theodoratou, E., Paschos, A., Magalon, A., Fritsche, E., Huber, R., and Bock, A. (2000) Nickel serves as a substrate recognition motif for the endopeptidase involved in hydrogenase maturation. *Eur. J. Biochem. 267*, 1995−1999.
39. Getzoff, E. D., Tainer, J. A., Weiner, P. K., Kollman, P. A., Richardson, J. S., and Richardson, D. C. (1983) Electrostatic recognition between superoxide and copper, zinc superoxide dismutase. *Nature 306*, 287−290.
40. Sines, J., Allison, S., Wierzbicki, A., and McCammon, J. A. (1990) Brownian dynamics simulation of the superoxide-superoxide dismutase reaction: iron and manganese enzymes. *J. Phys. Chem. 94*, 959−961.
41. Allen, F. H. (2002) The Cambridge Structural Database: a quarter of a million crystal structures and rising. *Acta Crystallogr. B 58*, 380−388.
42. Castagnetto, J. M., Hennessy, S. W., Roberts, V. A., Getzoff, E. D., Tainer, J. A., and Pique, M. E. (2002) MDB: the Metalloprotein Database and Browser at The Scripps Research Institute. *Nucleic Acids Res. 30*, 379−382.
43. Kruger, H. J., Peng, G., and Holm, R. H. (1991) Low-potential nickel(III,II) complexes−new systems based on tetradentate amidate thiolate ligands and the influence of ligand structure on potentials in relation to the nickel site in [nife]-hydrogenases. *Inorg. Chem. 30*, 734−742.
44. Holm, R. H., Kennepohl, P., and Solomon, E. I. (1996) Structural and functional aspects of metal sites in biology. *Chem. Rev. 96*, 2239−2314.
45. Darnault, C., Volbeda, A., Kim, E. J., Legrand, P., Vernede, X., Lindahl, P. A., and Fontecilla-Camps, J. C. (2003) Ni-Zn-[Fe4-S4] and Ni-Ni-[Fe4-S4] clusters in closed and open subunits of acetyl-CoA synthase/carbon monoxide dehydrogenase. *Nat. Struct. Biol. 10*, 271−279.
46. Doukov, T. I., Iverson, T. M., Seravalli, J., Ragsdale, S. W., and Drennan, C. L. (2002) A Ni-Fe-Cu center in a bifunctional carbon monoxide dehydrogenase/acetyl-CoA synthase. *Science 298*, 567−572.
47. Guan, Y., Hickey, M. J., Borgstahl, G. E., Hallewell, R. A., Lepock, J. R., O'Connor, D., Hsieh, Y., Nick, H. S., Silverman, D. N., and Tainer, J. A. (1998) Crystal structure of Y34F mutant human mitochondrial manganese superoxide dismutase and the functional role of tyrosine 34. *Biochemistry 37*, 4722−4730.
48. Vance, C. K., and Miller, A. F. (1998) A simple proposal that can explain the inactivity of metal-substituted superoxide dismutases. *J. Am. Chem. Soc. 120*, 461−467.
49. Madura, J. D., Briggs, J. M., Wade, R. C., Davis, M. E., Luty, B. A., Ilin, A., Antosiewicz, J., Gilson, M. K., Bagheri, B., Scott, L. R., and Mccammon, J. A. (1995) Electrostatics and diffusion of molecules in solution−simulations with the University-of-Houston Brownian dynamics program. *Comput. Phys. Commun. 91*, 57−95.
50. Sanner, M. F., Olson, A. J., and Spehner, J. C. (1996) Reduced surface: an efficient way to compute molecular surfaces. *Biopolymers 38*, 305−320.

BI0496081